

# Measuring the dynamical length of galactic bars

Michael S. Petersen,<sup>1</sup>★ Martin D. Weinberg,<sup>2</sup> Neal Katz<sup>2</sup>

<sup>1</sup>*Institute for Astronomy, University of Edinburgh, Royal Observatory, Blackford Hill, Edinburgh EH9 3HJ, UK*

<sup>2</sup>*Department of Astronomy, University of Massachusetts at Amherst, 710 N. Pleasant St., Amherst, MA 01003*

24 May 2023

## ABSTRACT

We define a physically-motivated measure for galactic bar length, called the *dynamical length*. The dynamical length of the bar corresponds to the radial extent of the orbits that are the backbone supporting the bar feature. We propose a direct observational technique using integral field unit spectroscopy to measure it. Identifying these orbits and using the dynamical length is a more faithful tracer of the secular evolution and influence of the bar. We demonstrate the success of the metric for recovering the maximal bar-parenting orbit in a range of simulations, and to show its promise we perform its measurement on a real galaxy. We also study the difference between traditionally used ellipse fit approaches to determine bar length and the dynamical length proposed here in a wide range of bar-forming  $N$ -body simulations of a stellar disc and dark matter halo. We find that ellipse fitting may severely overestimate measurements of the bar length by a factor of 1.5–2.5 relative to the extent of the orbits that are trapped and actually comprise the bar. This bias leads to overestimates of both bar mass and the ratio of corotation radius to bar length, i.e. the bar speed, affecting inferences about the evolution of bars in the real universe.

**Key words:** galaxies: Galaxy: halo—galaxies: haloes—galaxies: kinematics and dynamics—galaxies: evolution—galaxies: structure

## 1 INTRODUCTION

A bar feature in a disc galaxy is made up of stars on particular orbits. Barred galaxies with stable bars must include the parenting  $x_1$  family of orbits (Contopoulos & Papayannopoulos 1980; Binney & Tremaine 2008). The  $x_1$  orbits can come in a variety of flavours, but the salient features are the same: elongated orbits with coherent apocentres. It is these coherent apocentres that give the strong ‘bar’ appearance.

In observations, one typically measures stellar bar structures in galaxies by fits using simple ellipses (see e.g. Kruk et al. 2018, for a large sample). Using isophotes, one places a series of increasing semi-major axis ellipses on the image of a barred galaxy. One uses the ‘best-fit’ ellipse, chosen based on some criteria such as the ellipse with the maximum ellipticity, to inform the a fundamental property of a bar: its length. Unfortunately, simulators have also seized on ellipse fits as a means to measure and compare galaxies<sup>1</sup>. For galaxy evolution studies, simply computing the ellipse-measured bar statistics and looking for relationships with other galaxy properties may confound, or at worst, mislead inferences about the nature of galaxy

evolution. Further, many different ellipse-determination schemes exist in the literature.

Bars are composed of orbits that are trapped in their own potential and ellipse fitting can include material that is not trapped and therefore not part of the bar. In fact, as we show in later sections, such material can overwhelm ellipse fitting methods. Hence, it is not clear what information the ellipse measures contain about the *dynamics* of the system. A variety of works have sought connections between observational characteristics of ellipse-measured bars and galaxy evolution. The general picture is that (1) bars are fast, that is, their length is some appreciable fraction of the corotation radius of a galaxy (Pérez et al. 2012; Garma-Oehmichen et al. 2022), (2) bars are redder than their host discs (Kruk et al. 2018), and (3) bars are long-lived, both from studies of the Milky Way (Bovy et al. 2019) and observations of high-redshift bars (Hodge et al. 2019).

The recent proliferation of studies using integral field units (IFUs) to image barred galaxies has ushered in a new era, where the kinematics of a barred galaxy can be studied. Various works have used the Tremaine-Weinberg method (Tremaine & Weinberg 1984) and IFU data to measure the pattern speed of bars (see the recent data sample for MaNGA galaxies in Guo et al. 2019). The typical finding is that bars rotate ‘fast’, signified by the ratio of the corotation radius to the length of the bar being significantly larger than unity (Debattista & Sellwood 1998). The theoretical relevance of ‘fast’ vs ‘slow’ or more generally the ratio  $\mathcal{R} \equiv R_{\text{CR}}/R_{\text{bar}}$  is that one requires  $\mathcal{R} \geq 1$  for orbits to reinforce a bar potential and, therefore, be trapped. Empirically, bars in simulations tend to

★ michael.petersen@roe.ac.uk

<sup>1</sup> Some studies, both observational and theoretical, use surface density Fourier measures to constrain the size of the bar; these measurements suffer from the same sorts of biases and ambiguities as ellipse fits. See, e.g. Frankel et al. (2022) for a comparison between simulations and observations using Fourier measurements.

form with  $\mathcal{R} \approx 1$  and change owing to torques thereafter. However, resolved stellar velocity fields from IFUs hold more information about the orbital content of a galaxy. The  $x_1$  orbit family has a unique velocity signature, in that the maximum radial turning points (apsides) coincide with the bar major axis.

Given that the ‘fast versus slow’ bar dichotomy is based on measuring the length of the bar, the length of the bar has particular importance for studies of bar evolution. In this paper, we present a diagnostic that can measure the maximal extent of the  $x_1$  orbits by looking for a unique velocity signature. We calibrate the technique against an evolving barred-galaxy simulation that has already been extensively studied in [Petersen et al. \(2021, hereafter Paper I\)](#) and [Petersen et al. \(2019, hereafter Paper II\)](#).

This paper is organised as follows. In Section 2, we introduce the dynamical length of the bar and briefly describe the simulation, along with relevant findings for the simulation from previous work ([Paper I](#)). In Section 3, we compare global measurements of the simulation: a direct comparison of ellipse fitting and dynamical measurements from orbital analysis. This section also presents a kinematic technique with which we determine the true length of orbits that form the backbone of the bar. We apply the measurement methods to an observed galaxy in Section 4. We discuss the findings in the context of galaxy evolution studies in Section 5 and conclude in Section 6. Appendix A explores other variations of our approach to determine the dynamical bar length, Appendix B explores a wider range of ellipse fitting techniques, and Appendix C applies our method to a wide range of bar simulations to show its robustness.

## 2 THE DYNAMICAL LENGTH OF A BAR

To validate our later application to IFU data, we first apply the presented techniques to a simulation of a disc galaxy that forms a bar. One may apply the techniques to any simulation of a disc galaxy that forms a bar, and the results can be validated as long as one can extract a potential. For this work, we use a previously-analysed simulation from [Paper I](#): the ‘cusp’ simulation. As we evolved using the basis function expansion  $N$ -body code `EXP` ([Weinberg 1999; Petersen et al. 2022](#)), extracting the potential for further analysis is straightforward through a representation by basis functions.

The simulation we consider features an exponential stellar disc embedded in a live NFW dark matter halo. When describing the disc throughout this work, we will work in unitless ‘scale length’ units, using the initial scale length of the exponential stellar disc,  $R_d$ , to facilitate the translation between simulations and observations. For a Milky Way-like galaxy, a scale length is approximately 3 kpc.

### 2.1 The theoretical basis for the dynamical length

The maximum extent of trapped orbits that comprise the backbone of the bar (the  $x_1$  family; [Contopoulos & Papayannopoulos 1980; Binney & Tremaine 2008](#)), sets the *dynamical length* of the bar. If one were to axisymmetrise the  $x_1$  orbits in a given barred galaxy, the bar would disappear, whereas anything outside of the  $x_1$  family can be shuffled without a significant reduction in the self-gravity of the bar. Furthermore, outside of the bar dynamical length, the orbits may *gain* angular momentum (from the bar), resulting in a phase-lagged spiral structure. This is in contrast to the classic secular evolution picture where bar orbits *lose* angular momentum, resulting in a bar pattern speed decrease (slowing). The material outside of the dynamical length responds to the  $x_1$  orbit family, appearing as an elliptical distortion of untrapped stars lingering

near the bar. This material would not remain ‘bar-shaped’ in the absence of the trapped  $x_1$  orbits. Such orbits can greatly change the inferred bar lengths using ellipse fits.

The dynamical length of a bar is a more informative metric for the evolution of the bar, as it more closely approximates the self-gravity in the bar feature. Using the dynamical length, and hence the truly trapped orbits, to estimate the mass of the bar will also result in a more accurate estimate for the bar mass, something that we will return to in future work.

The dynamical length of the bar can provide constraints on both the pattern speed and the mass distribution of the inner galaxy. This amounts to finding the maximal  $x_1$  orbit, which may be possible to directly determine through kinematics. The dynamical length can also help determine the location of resonances that may feed the bar, i.e. add mass and length to the bar through the trapping of new orbits.

### 2.2 Identification of bar-parenting orbits in self-consistent potentials

In [Paper I](#), we analysed bar membership in this simulation through the clustering of the radial turning points, or apses, for a given orbit. Orbits ‘trapped’ by the bar’s gravity will librate about the position angle of the bar’s major axis, and will appear as (nearly) closed orbits in the frame of the bar. In this work, we primarily considered orbits that contribute to the structure of the bar: the  $x_1$  family associated with the inner Lindblad resonance (ILR;  $2\Omega_\phi - \Omega_r = 2\Omega_p$ , where  $\Omega_p$  is the pattern frequency of the bar). These orbits comprise the ‘backbone’ of the bar and are eccentric orbits elongated along the bar axis.

Briefly described (see [Paper I](#) for details), our method isolates the turning points in an orbit by looking for local maxima in radius. Using a rolling average of 20 apses<sup>2</sup> in Cartesian coordinates that we transform to a frame co-rotating with the bar position angle,  $\theta_{\text{bar}}$ , we compute the position angle for the centre of two  $k$ -means-derived clusters relative to the bar, taking the maximum of the two values. The desire to align with the two ends of the bar motivates our choice of two clusters. In addition to the cluster position angles, we compute the variance in the position angle relative to the cluster centre over the 20 apses,  $\sigma_{\theta_{\text{bar},20}}$ . These two quantities alone allow for a successful classification of orbits into the  $x_1$  family if we limit the average apse position to be  $\langle \theta_{\text{bar}} \rangle \leq \pi/8$  and the variance to be  $\sigma_{\theta_{\text{bar},20}} \leq \pi/16$ . From an empirical examination of the orbits, we estimate a contamination rate in the  $x_1$  family of approximately 1 per cent. This uncertainty does not change any of the results we present in this work.

We plot the turning radius of the longest  $x_1$ , identified using the above method, as the black curve in the upper panel of Figure 1. In [Paper I](#) we identified three stages of bar evolution in this simulation: the shortlived assembly phase when the bar first forms, the growth phase when the bar grows in the length and mass, and the steady-state phase when the bar does not evolve much at all. The length of the  $x_1$  orbits grows rapidly through the first time unit (assembly phase), slowly through the second (growth phase), and essentially not at all after that (steady-state phase). All together, the dynamical length appears to show little evolution over the bulk of the simulation. However, we emphasise that this model is missing several elements of realism for comparison to real galaxies, and should, therefore, be

<sup>2</sup> We determined the rolling average of 20 empirically to be a sweet spot in a trade-off between time resolution and signal-to-noise.

treated instead as a testing ground for theoretical insights, such as the identification of the  $x_1$  population. In the next section, we present measurements of the bar in all three phases (at  $T = 0.6, 2.0, 4.0$ ), to explore when one expects our method to work well. We investigate additional simulations in a phase-agnostic manner in Appendix C.

With the importance of  $x_1$  orbits in mind, as well as the observationally-unfortunate necessity of a potential model to conclusively identify them, we endeavour to find an *indicator* that can track the extent of the maximal  $x_1$  orbit in an observationally-friendly and computationally inexpensive manner.

### 3 OBSERVATIONAL BAR MEASUREMENT TECHNIQUES

In this section, we compare two methods to parameterise the size of the bar: measurement of the maximum radius of the trapped  $x_1$  orbits that support the bar potential and traditional ellipse fitting to the isophotes of surface density.

#### 3.1 Bar Measurement via Kinematic Signatures

Paper I demonstrated that  $x_1$  orbits dominate the population of the bar, particularly at later stages of bar evolution. In turn, this suggests that such orbits may also dominate integrated kinematic measurements. Using our theoretical understanding of  $x_1$  orbits, we can make predictions for the velocity signatures of these orbits. Because the tangential velocity of the bar orbits reach a minimum at the end of the bar, the velocity should show a marginally lower amplitude at the end of the bar than that expected for ordinary disc orbits. Figure 2 shows the surface density (upper panels) and velocity fields (lower panels) for the three model potentials studied in this paper, confirming by eye that the velocity field features ‘dimples’ as a result of the bar. The dimples are an  $m = 4$  signal that arises from the libration signature of the  $x_1$  orbits. The ability to distinguish a trapped  $x_1$  orbit from an untrapped orbit will be largest at the extrema of the libration oscillation. In other words, the dimple is an arc of libration turnarounds. In the case of the perfect parent  $x_1$  orbit, this feature would be a point, but for librating orbits the dimples smear into an arc with four-fold symmetry.

Our developed technique harnesses this feature as a diagnostic of the maximal extent of  $x_1$  orbits. Given a continuous velocity field tangential to the bar axis (such as from an integral field unit), the signal from trapped  $x_1$  bar orbits will be low compared to disc orbits and will, therefore, be largest where the discrepancy between the bar orbits and the disc orbits is largest, i.e. at the ‘four corners’ of the bar. This suggests that a kinematic metric using four-fold  $m = 4$  symmetry will reveal the largest differences between the bar and disc velocities. The difference between the velocities of bar and disc orbits will be negative at the corners of the bar and so we expect the  $m = 4$  velocity moment tangential to the bar,

$$v_{4\perp} = \frac{1}{N} \sum_{i=0}^N v_{\perp,i} \cos(4\phi_i), \quad (1)$$

to be appreciably negative. The quantity  $v_{\perp,i}$  is the velocity perpendicular to the bar for an individual particle or pixel; in our test cases where the bar is aligned with the  $x$  axis, the perpendicular velocity is simply  $v_y$ . As the bar slows, we expect the  $v_{4\perp}$  quantity to become even more extreme since the velocity between the untrapped disc orbits and the bar pattern speed becomes more discrepant (Paper I). In Equation (1), we compute the sum for a set of particles; here

we choose particles in annuli to obtain  $v_{4\perp}(R)$  as a function of cylindrical radius.

To test the significance of the signal relative to that of the bar, we compare the  $m = 2$  and  $m = 4$  velocity moments,  $v_{4\perp}$  to

$$v_{2\perp} = \frac{1}{N} \sum_{i=0}^N v_{\perp,i} \cos(2\phi_i). \quad (2)$$

This suggests a procedure to observationally determine the maximal extent of  $x_1$  orbits, which we call the  $x_1$  *velocity method*, as follows:

(i) Compute the *magnitude* of the velocity perpendicular to the bar,  $v_{\perp}$ , for each particle  $i$ .

(ii) Compute the  $m = 2$  and  $m = 4$   $x_1$  velocity components as a function of radius,  $v_{2\perp}(R_j)$  and  $v_{4\perp}(R_j)$ , partitioning the particles into bins delineated by annular radii  $\{R_j\}$ . One must take care not to reduce the signal-to-noise ratio by choosing annuli that are too narrow relative to the spatial resolution<sup>3</sup>. We suggest a minimum annular radius of  $\delta r = 10\delta x$ , where  $\delta x$  is the pixel scale.

(iii) Locate the radius for the min  $\{v_{4\perp}(R_j)/v_{2\perp}(R_j)\}_j$ . As long as  $\min \{v_{4\perp}(r_j)/v_{2\perp}(r_j)\}_j$  is significant<sup>4</sup>, this method is reliable and the minimum approximately equals the maximal extent of the  $x_1$  orbits.

To use this metric, one requires high spatial and velocity resolution, coupled with a modest inclination. As a general guideline, this requires a spatial resolution of  $\delta x = 0.05R_d$ , where  $R_d$  is the disc scale length, for a galaxy at an inclination of  $45^\circ$ , and requires a velocity resolution of  $0.05v_{\max}$ , where  $v_{\max}$  is the maximum circular velocity, to determine the  $v_{4\perp}/v_{2\perp}$  metric. For a MW-like galaxy, this translates to an  $\approx 10 \text{ km s}^{-1}$  velocity resolution and a 150 pc spatial resolution.

In Figure 3, we show this diagnostic for the model potentials using the above method. As expected, all three models show negative  $v_{4\perp}/v_{2\perp}$  values, driven by the effect at the corners of the bar. As the diagnostic requires binning to compute  $v_{4\perp}/v_{2\perp}$ , we sample each model with a range of bin widths, increasing the number of bins. For each measurement in a different bin, we measure the root variance via a jackknife procedure, repeatedly randomly sampling the particles in the bin<sup>5</sup>. The bins are then shown as circles whose radii correspond to the root variance of the individual observation. The outer envelope of the circles gives an approximate measure of the uncertainty in determining the underlying curve.

The signal is very strong during the growth and steady-state phases, with only a weakly discernible minima signature near the end of the bar in the assembly phase. One expects a low signal in the assembly phase since the kinematic feature results from trapped, evolved orbits that develop at the start of the growth phase. Even in the case of marginally significant detections, the  $v_{4\perp}/v_{2\perp}$  method results in a more accurate bar length determination compared to methods using ellipse fits. While we restrict our measurements to the  $m = 2$  and  $m = 4$  components of the velocity field, we have

<sup>3</sup> In practice, we estimate the uncertainty on the values of  $v_{2\perp}(R_j)$  and  $v_{4\perp}(R_j)$  via a jackknife procedure, taking  $\sqrt{N_j}$  samples in each bin, where  $N_j$  is the number of particles in the bin, and compute the root variance for each set of Fourier coefficients.

<sup>4</sup> We do not currently have a quantitative measure of the significance, but in practice we have found the minima are unambiguous. We discuss strategies for estimating the uncertainty below.

<sup>5</sup> This will not be strictly possible in real observations, but we perform the procedure here to test the robustness of the binning.

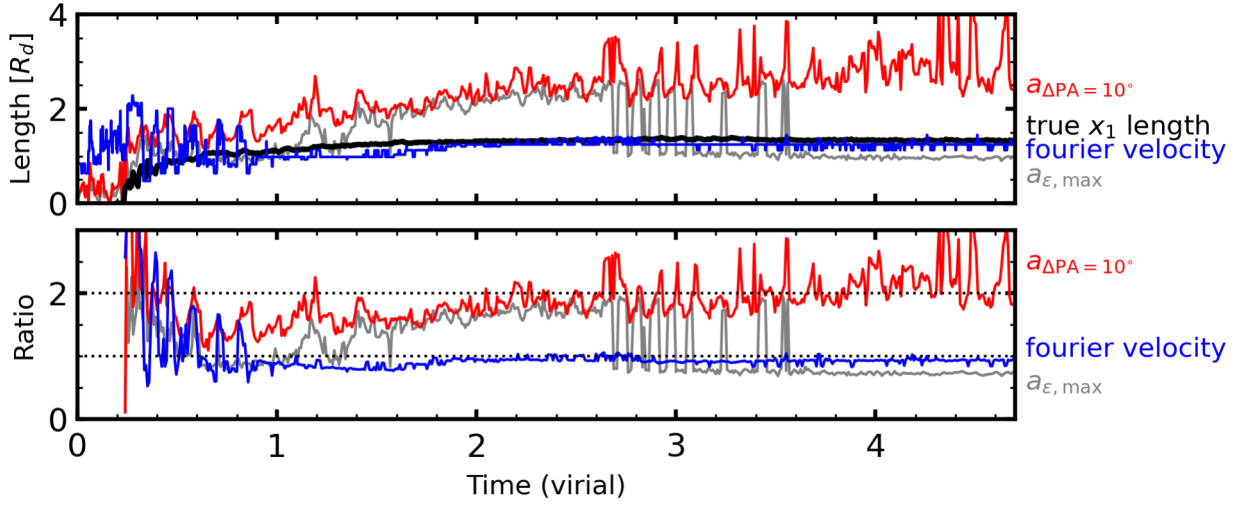


**Figure 1.** Upper panel: The length of the bar in disc scale lengths, measured using four different techniques: maximal  $x_1$  extent, two different ellipse fits, and our  $x_1$  velocity diagnostic, versus time. The  $x_1$ -derived length is the black curve. The simulation ellipse-fit-derived length from maximum ellipticity is shown in grey and the position angle length is in red. The  $x_1$  velocity diagnostic is shown in blue. Lower panel: The ratio of the ellipse-fit-derived length to the  $x_1$ -derived length versus simulation time for the measurement techniques in the upper panel (same colour scheme). The  $x_1$  velocity diagnostic is the least biased measure of the true  $x_1$  length.

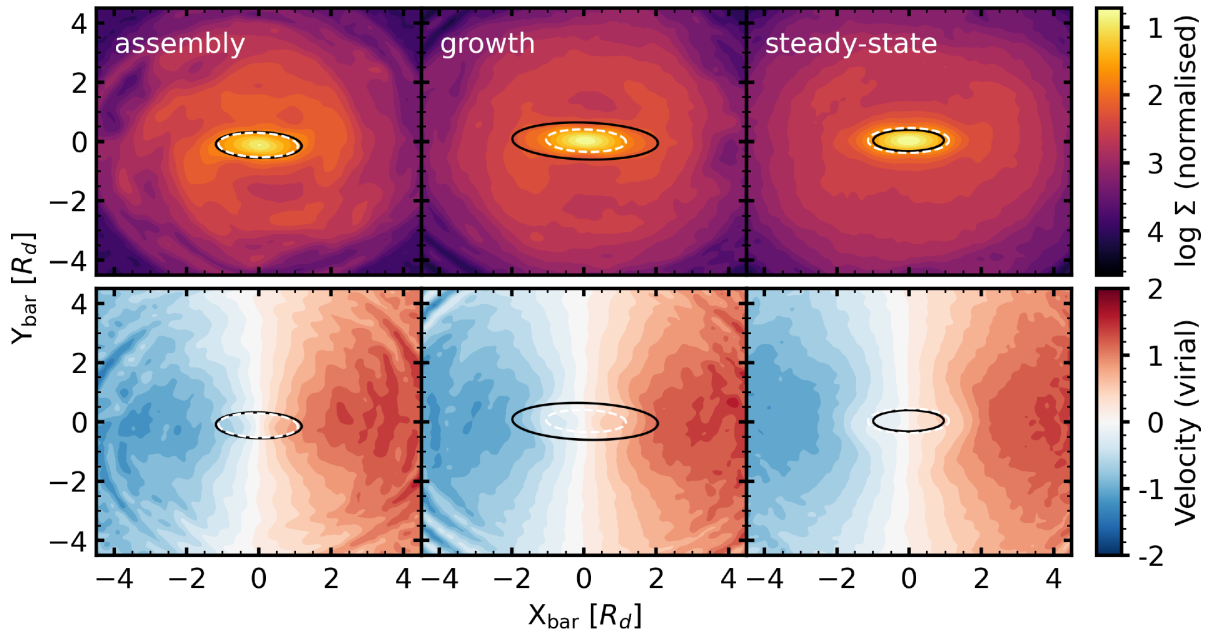


**Figure 2.** Upper panels: Log surface density, in normalised units, for the three evolutionary phases in the simulation: assembly, growth, and steady-state. Lower panels: The velocity field in the direction tangential to the bar, for the three phases in the upper panels. The white dashed ellipses show the maximum extent of the trapped  $x_1$  orbits, which coincides with the dimple in the velocity field in the growth and steady-state phases, as calculated from  $v_{4\perp}/v_{2\perp}$  for the velocity field tangential to the bar (see text). The black dashed ellipses show the maximum ellipticity ellipse for the bar from the surface density plot alone.

also tested the inclusion of higher order harmonics to improve the quality of detections, as described in Appendix A.

In the upper panel of Figure 1, we plot the length of the bar derived using the  $x_1$  velocity method as a blue curve. In the lower panel of Figure 1, we compute the ratio of this estimated length to the actual maximal  $x_1$  length and it accurately finds the true maximal  $x_1$  orbit length. Hence, this technique is a simple way to probe

for the dominant barred galaxy orbit and determine a dynamically-relevant length for a bar, and also a more accurate measure of the trapped fraction in galaxies. The technique does require a continuous velocity field, but these are becoming readily available with IFUs. In Appendix C, we apply our  $x_1$  velocity method to a wide sample of barred galaxy simulations to confirm that our method remains robust.



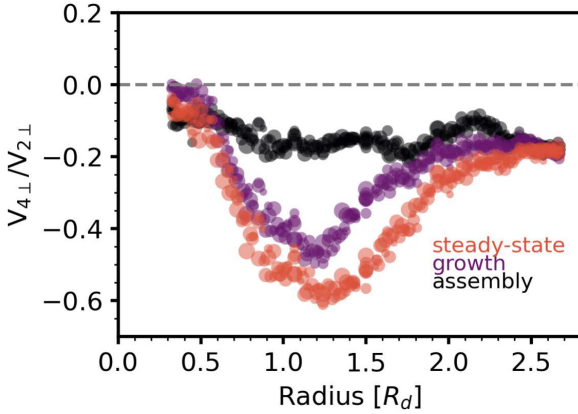


**Figure 3.** Demonstration of the  $x_1$  velocity method for finding the dynamical length of a bar. Each coloured set of circles, corresponding to repeated samplings using different binning, is the Fourier indicator computed for a different phase of the bar evolution. The outer envelope of the circles gives a measure of the uncertainty. The size of the circle corresponds to the root variance of the individual observation.

### 3.2 Bar Measurement via Ellipse Fits

To place our results in context, we compare with ellipse fits to bar isophotes. Many studies fit ellipses to bar isophotes (e.g. Muñoz-Mateos et al. 2013; Laurikainen et al. 2014; Kim et al. 2015; Erwin & Debattista 2016; Kruk et al. 2018)<sup>6</sup>. The various ellipse measurements have known discrepancies. In an example, Athanassoula & Misiriotis (2002) demonstrate that different ellipse methods applied to the same galaxy can lead to variations of up to 35 per cent in the measured bar length.

Following on this work, Muñoz-Mateos et al. (2013) measured bar lengths in the S<sup>4</sup>G sample (Sheth et al. 2008) using four different ellipse metrics derived from either the ellipticity profile or position angle of the best-fit ellipse at a given radius, reproduced here for clarity: (1)  $a_{\epsilon,\max}$ , the radius where the ellipticity of the bar is maximum, (2)  $a_{\epsilon,\min}$ , the first local minimum after the maximum, (3)  $a_{\Delta\epsilon=0.1}$ , the radius where the ellipticity drops by 0.1 compared to the maximum ellipticity, and (4)  $a_{\Delta\text{PA}=10^\circ}$ , the radius where the position angle differs by  $>10^\circ$  from the position angle at the maximum ellipticity.

The range of options for classifying the length of the bar highlights the challenge of algorithmically finding a bar length based on ellipse fits<sup>7</sup>. It is generally claimed in the literature that  $a_{\epsilon,\max}$  may be thought of as a minimum bar length (e.g. Athanassoula & Misiriotis 2002; Martinez-Valpuesta et al. 2006;

<sup>6</sup> While some papers have recently moved to Fourier-based decompositions of the bar (e.g. Guo et al. 2019; Frankel et al. 2022), such measurements of bars are subject to the same biases and algorithmic-consistency challenges as ellipse fits, so the general spirit of this section still holds.

<sup>7</sup> Many studies have made use of visually-determined bar lengths, including Galaxy Zoo (Hoyle et al. 2011) and S<sup>4</sup>G (Sheth et al. 2008). While visually measuring a bar length is a quick process for individual galaxies, the method does not necessarily trace an isodensity surface and often offers no errors on individual measurements. Hoyle et al. (2011) found that individual observers report approximately a 6 per cent deviation relative to the mean of all observers who classify a bar length. Connecting to ellipse-fit methods, (Herrera-Endoqui et al. 2015) demonstrated that visual fits to bar lengths are roughly comparable to  $a_{\epsilon,\max}$ .

Muñoz-Mateos et al. 2013). Therefore, some studies have used the maximum ellipticity to identify bars. For instance, in a recent paper studying bars in JWST early release fields (Guo et al. 2022), the maximum ellipticity value defines the bar length. However, no study that we have identified to-date has performed orbit decompositions to find the true dynamical backbone of the bar. And as we shall see below, even the assumed lower limits for bar length are overestimates of the maximal  $x_1$  length.

To perform a comparison between measurement techniques, we fit ellipses to our simulated galaxy. We use `elliptical`, a purpose-built ellipse fit Python package that implements many procedures common to ellipse fits of barred galaxies. In brief, `elliptical` accepts an image, then uses `scikit-image.find_contours` (van der Walt et al. 2014), a marching-squares algorithm, on the face-on image of the galaxy to determine the position of isophotal contours given a surface density. Then `elliptical` computes the best fit ellipses from the matrix representation of conic sections<sup>8</sup> for a range of isophotal values in the vicinity of the bar. Given the set of fit ellipses, we can select different criteria for the bar length. Examples are given in Appendix B. In practice, we select the maximum ellipticity as the bar length, for reasons that will become clear below. As a second comparison, we select an alternate bar length as the smallest ellipse where the position angle has changed by  $10^\circ$  from the position angle at maximum ellipticity. In the upper panel of Figure 1, we plot these as the grey curve (maximum ellipticity length) and the red curve (position angle- derived length). In the lower panel of Figure 1, we compute the ratio of the ellipse-derived measures to the maximal  $x_1$  length.

We find that selecting different criteria such as the maximum ellipticity or a threshold in position angle variation does not qualitatively change our results; all ellipse measures from (Muñoz-Mateos et al. 2013) return values within approximately 30 per cent, in agreement with Athanassoula & Misiriotis (2002). For a more thorough introduction to measuring bar lengths, we refer the reader to Erwin (2005) for an observationally motivated viewpoint, and Athanassoula & Misiriotis (2002) for a theoretically motivated viewpoint.

### 3.3 Why do the techniques return different results?

If bars are made of elongated, coherent orbits, and orbits make the elongated, coherent bar structures that may be traced by ellipse fits, why do the two methods give different results? In this section, we describe orbits that bias the ellipse fits of bars and demonstrate how ellipse fitting methods may overestimate the length of the bar.

Figure 2 summarises our velocity moment method as compared to standard ellipse fits. The upper panels of Figure 2 show the surface density during the three identified phases of bar evolution, and the lower panels show the y-component of the velocity (perpendicular to the bar) for each of the three phases.

In each phase, we plot the standard technique (ellipticity drop) best-fit ellipse in dashed black. The ellipse that corresponds to the minimum of  $v_{4\perp}/v_{2\perp}$  is shown in dashed white. As shown in Figure 3, while we compute a minima in the  $v_{4\perp}/v_{2\perp}$  value for the assembly phase, the signal is fairly ambiguous, despite still

<sup>8</sup> Alternately, one can perform a least-squares fit to the contour level (e.g. Athanassoula et al. 1990), which provides an additional level of flexibility in fits, but we do not find a substantial difference in our ellipse fit measurements if we choose this technique versus the matrix representation.

giving a matching value to the maximal  $x_1$  length<sup>9</sup>. However, during the growth and steady-state phases, strong signals are observed in  $v_{4\perp}/v_{2\perp}$ , which clearly show the maximal extent of the  $x_1$  orbit family. The discrepancy between ellipse-fit lengths and the actual maximal  $x_1$  orbit radius can be significant.

Assuming a constant mass-to-light ratio, we apply the standard ellipse-fitting analysis to our simulations. We compute the face-on surface density at a resolution of  $0.025a$ , which for a MW-like galaxy corresponds to  $75 \text{ pc}$ <sup>10</sup>. We measure the length of the bar using a standard method: determine best-fit ellipses at many different surface densities and assign the bar length to the semi-major axis value,  $a$ , where the ellipticity drops below a certain threshold or has a discontinuity. Here, we choose the semi-major axis where the ellipticity  $e \equiv 1 - \frac{b}{a}$ , and  $b$  is the semi-minor axis value, first drops below 0.5. In practice, this is also the same location as the discontinuity in  $e$  that corresponds to the transition between bar-dominated contours and disc-dominated contours. We also have a dynamically-informed metric for the length of the bar: the maximum extent of the  $x_1$  family (Paper I). Figure 1 shows a comparison of the maximum  $x_1$  extent versus ellipse-fit derived bar lengths. In the upper panel, we show the bar lengths measured using both techniques. The two ellipse fit lengths in the simulation (grey and red curves) grow steadily at  $T < 1$ , except for a later shift to a new set of ellipses from the maximum ellipticity measurement ( $T > 3$ ). The growth roughly mirrors the trapped fraction growth, but when compared to the maximal extent of the  $x_1$  orbits (black), we see that this is an extreme overestimate for the length of the trapped component. The periodicity in the ellipse measurements results from the outer disc  $m=2$  disturbances, e.g. spiral arms, coincidentally aligning with the bar. At early times when the bar is forming, this can result in variations of nearly a factor of two. Even at later times in the simulation, the variation in ellipse-fit length is 25 per cent over short ( $\delta T = 0.1$ ) timescales owing to the  $m=2$  alignment.

The lower panel of Figure 1 summarises the overall results of our comparison. We plot the ratio of the ellipse-fit length to the maximal  $x_1$  length for the simulation. The ellipse-fit length is a large overestimate for the length of the  $x_1$  orbits at all times in the simulation, typically by a factor of 1.5, except during the assembly phase when the overestimate is a factor of two. Thus, the simulation reveals the ambiguity in ellipse-fit determinations of bars. Ellipse fits may be taken as a measure of the total mass distribution of the galaxy, not as the mass directly associated with the bar itself.

The gravity from the bar causes the untrapped disc orbits to linger along the bar position angle. This confuses metrics that are based on the shape alone, such as ellipse fits and Fourier-derived strengths. Typically, the length of the bar will be overestimated by 50 per cent. One needs an accurate length of the true bar orbits to observationally determine the pattern speed (e.g. Guo et al. 2019; Garma-Oehmichen et al. 2022). The dimensionless parameter  $\mathcal{R} \equiv R_{\text{CR}}/R_{\text{bar}}$  denotes the ‘slowness’ of the pattern speed. As discussed in Binney & Tremaine (2008), this parameter can be hard to measure in real galaxies for two reasons: (1) the bar does not have a sharp end, and (2) corotation does not have a clear definition for strong non-axisymmetric disturbances, e.g. a strong bar. However,

several studies have attempted to measure either the pattern speed or the dimensionless parameter to characterise the bar. Thus, an overestimate of the true dynamical length of the bar overestimates the pattern speed, sometimes significantly.

In Appendix C, we apply the ellipse fitting technique to a wide sample of barred galaxy simulations and confirm that these conclusions still hold. Other studies have found similar results, but for somewhat different reasons: Hilmi et al. (2020) points out that ellipse fits may encompass both bar and spiral activity, confusing dynamical information. Additionally the spiral arms may create real modulations in the bar feature, particularly the pattern speed. We do not find any obvious evidence for pattern speed modulation, and we can conclusively say that the length of the  $x_1$  orbits does not fluctuate on spiral-arm timescales when spirals are present in our model (primarily during the growth phase).

In conclusion: *if one must pick an ellipse fit measurement for the bar length, the maximum ellipticity is likely to be the best tracer of the  $x_1$  orbits.*

## 4 EXAMPLE APPLICATIONS

### 4.1 Utility for IFU surveys

As a proof of concept example, we apply our measurement technique to a Milky-Way-like galaxy measured in the MaNGA survey (Bundy et al. 2015). We select galaxy 8444-12703, a part of a Milky-Way-analogue subsample (Garma-Oehmichen et al. 2022). We perform the analysis purely on the MaNGA data cube. Using the log flux, we draw ellipses on the image. This bar is particularly interesting, as both a Milky Way analogue, but also for the unphysically-low measurement of the dimensionless bar pattern speed ratio  $\mathcal{R} = 0.9 \pm 0.2$  (Garma-Oehmichen et al. 2022). This low  $\mathcal{R}$  measurement owes to finding a large bar length of  $5.7 \pm 0.9$  arcseconds. This reported bar length corresponds to the maximum ellipticity radius, which is similar to the 5.8 arcsecond value returned by `elliptical` when computed on the MaNGA log flux image. We show the ellipse of constant surface density, measured by `elliptical`, as a black ellipse in both panels of Figure 4.

Using the deprojection values from (Garma-Oehmichen et al. 2022), and using `elliptical` to perform the deprojection, we rectify the velocities to be face on, with the bar aligned with the  $x$ -axis to find the velocity field perpendicular to the bar. Using this velocity field, we compute the velocity Fourier moments as a function of radius<sup>11</sup>. However, as this fit has been performed in the deprojected space, we must re-project the bar length onto the sky image. We do this using the inverse transformation matrix. Given the reprojected bar length, we identify the ellipse measured by `elliptical` which has the same semi-major axis length. This is shown as the white-dashed ellipse in both panels of Figure 4.

We find that our  $x_1$  velocity indicator suggests a maximal  $x_1$  length of  $4.1 \pm 0.3$  arcseconds, in contrast to the 5.8 arcseconds of the maximum ellipse. If we take the corotation radius at face value from Garma-Oehmichen et al. (2022), this change in bar length immediately raises the ratio  $\mathcal{R}$  to a more physical value, 1.3. Hence, our proof of concept example demonstrates that when IFU data is

<sup>9</sup> With the omniscience provided by simulations and the true calculation of the maximal  $x_1$  orbits, we see that the  $x_1$  track is not yet fully formed (the apsis precession that traps orbits into the bar is an ongoing process), and thus the technique will not, by definition, be informative.

<sup>10</sup> In practice, the ellipse fits are weakly dependent on the resolution, introducing approximately a 10 per cent error.

<sup>11</sup> As a measure of uncertainty, we sample the bin spacing several times and plot the resultant points scaling according to the root variance of individual measurements (as in Figure 3). The envelope of these measurements may be used to estimate the uncertainty. In practice, we find that a conservative estimate of the uncertainty is 15 per cent.

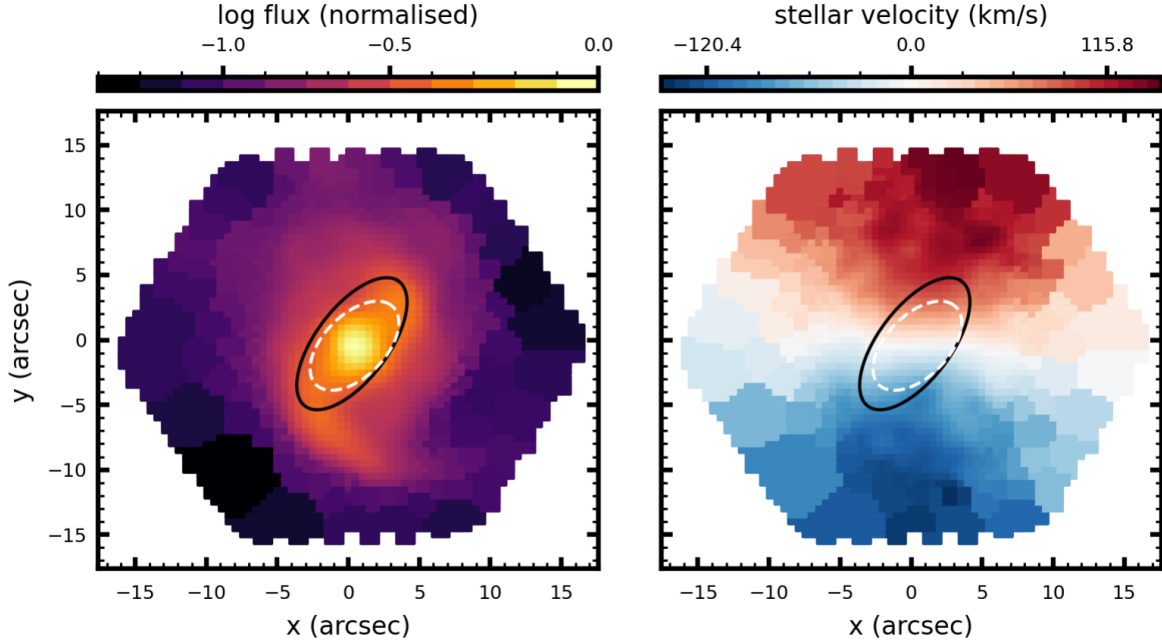


**Figure 4.** Left panel: log surface density, normalised to the central value, for the MaNGA galaxy 8444-12703. North is up, east is right (note that many display images are flipped with respect to the y-axis). Right panel: stellar velocity, in km/s. We show two ellipses in both panels: the black solid ellipse is the maximum-ellipticity ellipse drawn from a sample of ellipses fit to the isophotes. The white dashed ellipse is drawn from the same sample of ellipses fit to isophotes, but has been chosen as the ellipse with the semi-major axis that most closely matches the measured dynamical length of the bar.

present, the stellar velocity field may be used to additionally help constrain the dynamical length of the bar and its relationship with corotation.

An analysis of a larger sample of galaxies is beyond the scope of this work; in fact, this measurement may not be possible for a number of MaNGA galaxies owing to unavoidable limitations in their orientation (relating to uncertainties in projection), as well as instrumental effects such as the size of the IFU fibre field, the coarseness of the spatial sampling, correlated information between pixels, and signal-to-noise. Future work will have to perform a careful analysis of these considerations when applying our  $x_1$  velocity method to a wider range of galaxies, and automation may not be trivial. Here, we simply provide a proof-of-concept and evidence that our findings from a model galaxy appear to be applicable to Nature. We expect that the largest variation in our results compared to observational findings is likely the uncertainty in the inclination and the position angle of the line of nodes. cursory tests suggest that the introduction of the inclination and position angle of the line of nodes can cause a 20 per cent variation in the determinations of the maximal  $x_1$  orbit length.

Looking ahead, higher velocity and spatial resolution, potentially feasible using current instruments, makes a modest difference. Comparison with maximal  $x_1$  extents (computed in Paper I, as shown in Figure 1) shows that the minima of  $v_{4\perp}/v_{2\perp}$  is within 10 per cent of the maximal  $x_1$  orbit radius, making this technique a powerful discriminator of the dynamically-relevant maximal  $x_1$  orbit.

## 4.2 Insights for high-redshift bars

Given that the maximum ellipticity appears to be the most robust of the still biased ellipse based methods, as a tracer of the  $x_1$  pop-

Parameter	Literature Value	This paper
$\log \left( \frac{M}{M_\odot} \right)$	10.9	-
Bar Length (max. $\epsilon$ )	5.7 (arcsec)	5.8 (arcsec)
Bar Length (dynamical)	-	$4.1 \pm 0.3$ (arcsec)
Deprojected Bar Length	$5.0 \pm 0.7$ (kpc)	$3.6 \pm 0.5$ (kpc)
Disc PA	$4^\circ.0 \pm 0.6$	-
inclination	$37^\circ.2 \pm 1.2$	-
Bar angle	$31^\circ.7 \pm 9.5$	-
$\mathcal{R}$	$0.9 \pm 0.2$	$1.3 \pm 0.3$

**Table 1.** Parameters for MaNGA galaxy 8444-12703. The literature values come from Garma-Oehmichen et al. (2022), which measures the mean of the bar length to be  $R_\epsilon$ , the maximum ellipticity. The uncertainty is drawn from a lognormal distribution using  $R_{PA}$  (the radius at which the position angle changes by  $5^\circ$ ) as the upper limit. Deprojected bar length follows the procedure in Gadotti et al. (2007).

ulation, we suggest that analysis of barred-galaxy images would do better to trace the maximum ellipticity contour as a measure of the bar length. As a demonstration of how this measure may change published results, we measure the maximum ellipticity radius for six galaxies recently identified in JWST imaging as the highest-redshift bar candidates (Guo et al. 2022) using elliptical. We show the maximum-ellipticity ellipses overlaid on thumbnail images in Figure 5.

If we assume a similar potential down-scaling ratio from the maximum ellipticity fits and  $x_1$  lengths, we can attempt to recalibrate the bar length, with large uncertainties. Interpreting the range of overestimates from ellipse fits, we can estimate that some bar lengths may be overestimated by a factor of 2. To guide the eye on the factor of two reduction, we also add a constant surface density tracing ellipse with half the semimajor axis of the maximum



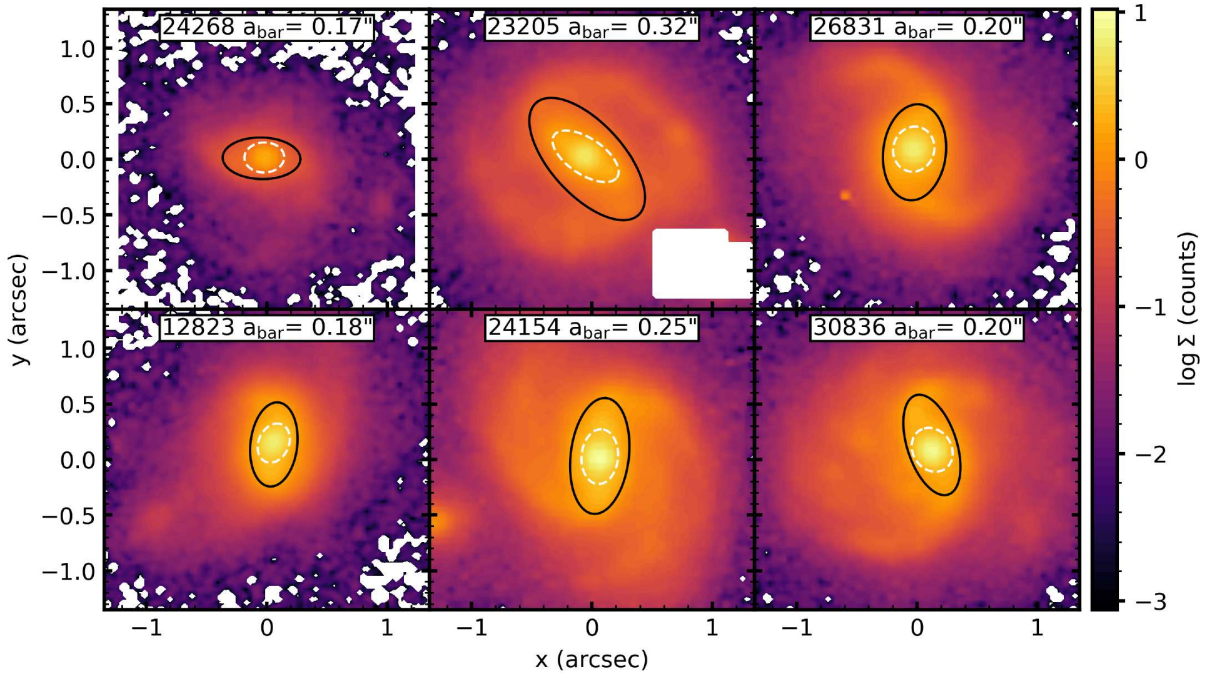


**Figure 5.** Six barred galaxies identified in Guo et al. (2022), with black ellipses indicating the maximum ellipticity measure. White dashed ellipses are the best-fit ellipse that has half the semi-major axis length of the black ellipse, in order to guide the eye as to possible bar length overestimations (see Section 4.2). Regions with negative flux are shown in white. We have masked a background galaxy in 23205 in order to show the galaxy with clearer contrast.

ellipticity ellipse as a dashed white ellipse. Several of these contours are quite circular; for some bars this may owe to the pixel size of JWST, but for others this may indicate that the bar feature is weak or potentially non-existent.

The galaxies in the CEERS dataset are prime candidates to observe using the integral field spectroscopy capabilities of JWST. Such analysis, seeking to identify  $x_1$  orbits in particular, are a necessary step in analysing the evolution of bars over cosmic time, possibly enabling statements about the evolutionary phase and determining whether these bars are created via instabilities in early-Universe discs, or whether the bars are more likely to be directly caused by interactions.

## 5 DISCUSSION

### 5.1 Comparison with fixed-potential analyses

The key quantity for the purposes of the analysis in this paper is the determination of the maximal  $x_1$  orbit turnaround radius. From fixed potential analyses, one can compute the theoretical maximum of the  $x_1$  family (e.g. Paper I). However, in self-consistent simulations, orbits will not necessarily reach the theoretical maximum, but will instead only extend to some fraction of it, as orbits near the theoretical maximum are susceptible to small perturbations that untrap them. This clouds the straightforward interpretation of fixed-potential analyses. The fixed-potential integration finds possible  $x_1$  orbits out to  $2R_d$ , while the maximal  $x_1$  found in the self-consistent

simulation at the same time is  $1.3R_d$ , a significant difference<sup>12</sup>. In light of this, methods that parameterise the length of the bar as the maximal theoretical  $x_1$  extent will overestimate the actual bar length (Martinez-Valpuesta et al. 2006).

Therefore, while a fixed-potential analysis has utility for characterising the possible orbital content, it is a more informative diagnostic of model bar evolution to probe the true extent of the  $x_1$  orbits. This is particularly important for comparison to observations, since one can only observe the maximum length of populated  $x_1$  orbits.

### 5.2 Use in cosmological simulations

The identification and measurement of bars in cosmological simulations is a similar, but not identical problem to the isolated model we study here. In the absence of the ability to resolve individual orbits, our  $x_1$  velocity method may be straightforwardly applied to cosmological simulations to both detect and parameterise bars. Given particle data, one may easily compute the Fourier velocity moments. We have not investigated the utility of our Fourier velocity method on particle-based data, but we expect that the method could be readily calibrated.

One such velocity-based bar measurement was attempted in Reddish et al. (2022), but without a robust sample of bars, the exercise was more useful as a validation that the method can be used

<sup>12</sup> Knowing where the maximum  $x_1$  orbit is located in  $r_{\text{apocentre}} - v_{\text{apocentre}}$  space, we can efficiently check our trapping analysis to ensure that we have not missed any elongated  $x_1$  orbits. We find that the  $k$ -means analysis efficiently recovers the most extended  $x_1$  orbits in the simulation, which are *not* the same extension as the theoretical maximum  $x_1$  orbit.



in tandem with surface density Fourier methods to detect the presence or absence of bars. In general, we endorse the practice of using velocity-based measurements to probe the presence of bars in simulations and observations, as examining the kinematics can reveal bar-supporting orbits, while also preventing false positives from ellipse fits to surface density.

Finding  $x_1$  orbits in cosmological simulations will be limited by temporal resolution. That is, the ability to resolve time-dependent orbits in cosmological simulations is typically a simple issue of the time between snapshots. Since the size of cosmological simulation outputs is large, the time spacing is usually large. However, a cosmological simulation invested in resolving the dynamics of bars could readily implement an on-the-fly  $x_1$  orbit finder using the apocentre clustering techniques presented in this paper and in Paper I. However, there is a concern that noise in the potential calculation in cosmological simulations, i.e. the forces, may cause unphysical orbit diffusion and hence further tests will be needed to see if our  $x_1$  velocity approach leads to valid bar measurements in these circumstances.

### 5.3 Comparison of observations and simulations

Given the prevalence of bars in galaxy surveys and the recent ability of cosmological simulations to form bars (Frankel et al. 2022), developing a common measurement system with which to interpret observations is paramount. However, one should not degrade the information in simulations to match the observations; rather one should work to find tracers of dynamically-relevant features in observations. In this work, we present a consistent dynamical measure for bars in simulations: the maximum extent of  $x_1$  orbits. We demonstrate that the maximum extent of  $x_1$  orbits may be recovered via the velocity field, and in particular using simple Fourier expansion measurements of the velocity field.

Simple ellipse fits (or surface density Fourier expansions) will be biased by disc orbits that are deformed (but not trapped) in response to the  $x_1$ -parented potential. These deformed orbits are not accurate tracers of bar evolution, and indeed appear to play little role in the evolution of model galaxies (Paper II) apart from feeding the growing bar (Paper I).

In a volume- and mass-limited study of local galaxies Erwin (2019) found a bimodal correlation between bar semimajor axis and stellar mass: at lower masses bar size is independent of stellar mass while at higher masses bar size strongly depends on the stellar mass. The dependence of stellar mass on galaxy size cannot explain the bar sizes at higher masses. More likely than not, these observations are confounded by their bar size definitions that depend on integrated light rather than orbit properties.

Similarly, over cosmic time, bar lengths strongly correlate with galaxy mass, but seem to show little to no evolution with redshift over  $0 < z < 0.84$  (Kim et al. 2021). Again, this may indicate that ellipse bar measurements are obscuring the true dynamical evolution.

In concert with a mass model, the maximum  $x_1$  extent can also be used to constrain the pattern speed of a barred galaxy. The idea of using the maximal extent of  $x_1$  orbits to characterise the Milky Way bar was recently studied by Lucey et al. (2022). However, one must take care when comparing mass models with observations, as the theoretical maximum  $x_1$  orbit is unlikely to be populated.

## 6 CONCLUSION

We introduced the concept of the *dynamical length* of a galactic bar: the maximum extent of the  $x_1$  orbit turnaround radius, the same orbits that parent the bar. The dynamical length provides a physically-motivated diagnostic that may be robustly compared across simulations and with observations, provided that the  $x_1$  orbits can be identified. With this motivation, we present an observational metric based on Fourier expansions of the galaxy velocity field to identify the maximum extent of  $x_1$  orbits in simulations and observations, which we call the  $x_1$  *velocity method*. IFU stellar velocity data enables locating orbits trapped in the bar feature using a simple Fourier-based velocity diagnostic,  $v_{4\perp}/v_{2\perp}$ . The bar-length bias caused by orbits deformed by the  $x_1$  potential but not actually trapped, can be mitigated through the inclusion of velocity data. The measurements above work equally well at all phases of barred galaxy evolution for a wide range of simulated bars.

We determined the dynamical length in a model galaxy and calibrated the observational metric against it. From this comparison, we determined that observational techniques currently used on both real galaxies and simulated galaxies are not measuring true bar lengths. We perform ellipse fits on our simulations, finding that typical ellipse-fit techniques systematically overestimate the maximum radial extent of the trapped bar orbits. We describe why ellipse based techniques overestimate the length of the bar. Such methods do not accurately represent the radial extent nor mass of orbits trapped in the bar, and are subject to unpredictable biases. As a proof of concept we successfully apply our new  $x_1$  velocity method to an observed galaxy to measure its dynamical bar length and as predicted ellipse fitting methods overestimate the true dynamical bar length.

There is scope for significant future work based on the technique presented here. In particular, while we applied our method to one example galaxy, large samples of barred galaxies have IFU data. Such work with samples of galaxies will undoubtedly have growing pains, and we expect to refine the method with further input for observational considerations. One additional line of study that may prove fruitful would be the combination of the indicators presented in this paper and the Tremaine-Weinberg method for pattern speed measurement (Tremaine & Weinberg 1984), which also uses the velocity field. Also desirable is a bin-free approach to finding the velocity-derived length. Currently we are using a ‘brute force’ approach to test different bin configurations, but a continuous function estimator would be much cleaner.

In the context of isolated simulated galaxies, we have not solved the problem of how to diagnose a bar in the ‘assembly’ phase; neither the velocity-field method nor  $x_1$  indicators work particularly well. However, the assembly phase is shortlived so our  $x_1$  velocity method should work well on most galaxies. With a focused study of bar formation in simulations, more robust  $x_1$  diagnostics during the assembly phase may be developed (see Appendix A for a discussion). We can, however, confidently assess that standard ellipse-fit measurements, including the maximum ellipticity, are overestimating the length of the bar during the assembly phase.

The observational techniques presented in this paper provide a promising avenue with which to study dynamical quantities for galactic bars. In turn, understanding bars may shed light on galaxy evolution as a whole as observations to increasingly higher redshift have shown that structure formation is commonplace in the early universe (Hodge et al. 2019; Guo et al. 2022).

## DATA AVAILABILITY

The `elliptical` code, which generated many of the measurements, is freely available on GitHub. The MaNGA and JWST data were both drawn from public data sets. Access to the simulation data will be provided upon reasonable request to the corresponding author.

## ACKNOWLEDGMENTS

MSP acknowledges support from a UKRI Stephen Hawking Fellowship. This work used cuillin, the Intitute for Astronomy’s computing cluster (<http://cuillin.roe.ac.uk>), partially funded by the STFC. We thank Eric Tittley for continued smooth operations. This project made use of *numpy* (van der Walt et al. 2011) and *matplotlib* (Hunter 2007). We used MARVIN (Cherinka et al. 2019) to access the MaNGA data cubes.

## REFERENCES

- Athanassoula E., Misiriotis A., 2002, *MNRAS*, **330**, 35  
 Athanassoula E., Morin S., Wozniak H., Puy D., Pierce M. J., Lombard J., Bosma A., 1990, *MNRAS*, **245**, 130  
 Binney J., Tremaine S., 2008, *Galactic Dynamics: Second Edition*. Princeton University Press  
 Bovy J., Leung H. W., Hunt J. A. S., Mackereth J. T., García-Hernández D. A., Roman-Lopes A., 2019, *MNRAS*, **490**, 4740  
 Bundy K., et al., 2015, *ApJ*, **798**, 7  
 Cherinka B., et al., 2019, *AJ*, **158**, 74  
 Contopoulos G., Papayannopoulos T., 1980, *A&A*, **92**, 33  
 Debattista V. P., Sellwood J. A., 1998, *ApJL*, **493**, L5  
 Debattista V. P., Sellwood J. A., 2000, *ApJ*, **543**, 704  
 Erwin P., 2005, *MNRAS*, **364**, 283  
 Erwin P., 2019, *MNRAS*, **489**, 3553  
 Erwin P., Debattista V. P., 2016, *ApJL*, **825**, L30  
 Frankel N., et al., 2022, *ApJ*, **940**, 61  
 Gadotti D. A., Athanassoula E., Carrasco L., Bosma A., de Souza R. E., Recillas E., 2007, *MNRAS*, **381**, 943  
 Garma-Oehmichen L., et al., 2022, *MNRAS*, **517**, 5660  
 Guo R., Mao S., Athanassoula E., Li H., Ge J., Long R. J., Merrifield M., Masters K., 2019, *MNRAS*, **482**, 1731  
 Guo Y., et al., 2022, *arXiv e-prints*, p. [arXiv:2210.08658](https://arxiv.org/abs/2210.08658)  
 Herrera-Endoqui M., Díaz-García S., Laurikainen E., Salo H., 2015, *A&A*, **582**, A86  
 Hilmi T., et al., 2020, *MNRAS*, **497**, 933  
 Hodge J. A., et al., 2019, *ApJ*, **876**, 130  
 Hoyle B., et al., 2011, *MNRAS*, **415**, 3627  
 Hunter J. D., 2007, *Computing in Science & Engineering*, **9**, 90  
 Kim T., et al., 2015, *ApJ*, **799**, 99  
 Kim T., Athanassoula E., Sheth K., Bosma A., Park M.-G., Lee Y. H., Ann H. B., 2021, *ApJ*, **922**, 196  
 Kruk S. J., et al., 2018, *MNRAS*, **473**, 4731  
 Laurikainen E., Salo H., Athanassoula E., Bosma A., Herrera-Endoqui M., 2014, *MNRAS*, **444**, L80  
 Lucey M., Pearson S., Hunt J. A. S., Hawkins K., Ness M., Petersen M. S., Price-Whelan A. M., Weinberg M. D., 2022, *arXiv e-prints*, p. [arXiv:2206.01798](https://arxiv.org/abs/2206.01798)  
 Martínez-Valpuesta I., Shlosman I., Heller C., 2006, *ApJ*, **637**, 214  
 Muñoz-Mateos J. C., et al., 2013, *ApJ*, **771**, 59  
 Navarro J. F., Frenk C. S., White S. D. M., 1997, *ApJ*, **490**, 493  
 Pérez I., Aguerri J. A. L., Méndez-Abreu J., 2012, *A&A*, **540**, A103  
 Petersen M. S., Weinberg M. D., Katz N., 2019, *MNRAS*, **490**, 3616  
 Petersen M. S., Weinberg M. D., Katz N., 2021, *MNRAS*, **500**, 838  
 Petersen M. S., Weinberg M. D., Katz N., 2022, *MNRAS*, **510**, 6201  
 Reddish J., et al., 2022, *MNRAS*, **512**, 160  
 Sheth K., et al., 2008, *ApJ*, **675**, 1141

Tremaine S., Weinberg M. D., 1984, *ApJL*, **282**, L5

Weinberg M. D., 1999, *AJ*, **117**, 629

van der Walt S., Colbert S. C., Varoquaux G., 2011, *Computing in Science & Engineering*, **13**, 22

van der Walt S., JL S., J N., F B., JD W., N Y., E G., T Y., 2014, *PeerJ*, **2**, e453

## APPENDIX A: OPTIMISING THE SIGNAL DETECTION

As the  $x_1$ -driven velocity signal is fundamentally a deviation from the quadrupole structure, seeking to find the four ‘corners’ of the bar in velocity space, one might naturally wonder whether a data-driven solution with increased sensitivity to the velocity ‘corners’ may be found. To this end, we tested a higher-order signal improvement scheme using principal component analysis (PCA). In practice, we computed the even harmonic orders for the (aligned) velocity field in annuli for even harmonic orders up to  $m_{\max} = 10$ , following

$$v_{m\perp} = \frac{1}{N} \sum_{i=0}^N v_{\perp,i} \cos(m\phi_i), \quad (\text{A1})$$

and constructed the matrix

$$\mathbf{X} = [v_{4\perp}, v_{6\perp}, v_{8\perp}, v_{10\perp}]^T, \quad (\text{A2})$$

where each  $v_{m\perp}$  is a list of values in each radius bin. We then decomposed the matrix  $\mathbf{X}$  using singular value decomposition,

$$\mathbf{X} = \mathbf{U}\mathbf{\Sigma}\mathbf{V}^T. \quad (\text{A3})$$

The columns of  $\mathbf{U}$  are the principal components, the first of which encodes the linear combination that makes up the strongest signal across the whole galaxy face<sup>13</sup>. The PCA reveals that the signal is indeed dominated by the  $m = 4$  signal, but higher order moments can contribute, particularly when the geometry of the bar is long and narrow. In the case of the primary model studied in this paper,  $v_{8\perp}$  contributes to the maximal signal at approximately the 20 per cent level during the assembly and growth phases – when the bar is particularly long and narrow. This may be thought of as a signal ‘boost’. We also checked for signal in the sine terms with the same processes (i.e. replacing cosine with sine in eq. A1), as well as odd  $m$  terms, and found no appreciable contribution. One could also test a cumulative power ratio strategy, where all non  $m = 2$  power is combined as an indicator of  $x_1$  orbits.

Overall, we find only marginal improvement against the naive  $v_{4\perp}/v_{2\perp}$  ratio, but for cases where the bar is particularly narrow, or the signal is weak, such a PCA process may prove useful. We expect such a technique may be more useful when measuring signals in real galaxies, where the inclination and observational uncertainty may obscure the signal.

## APPENDIX B: DETAILED ELLIPSE FIT DEMONSTRATION

Figure B1 shows ellipse-fit diagnostics for the primary simulation considered in this paper. This figure emphasises the ambiguity when performing ellipse fits, rather than the conceptually well-posed  $x_1$  velocity signal. In each face-on image, we also show the maximal  $x_1$

<sup>13</sup> By limiting the radius at which we evaluate  $v_{m\perp}$ , one could in principle isolate the strongest signal to be from the bar, but here we do not restrict the radius of evaluation.

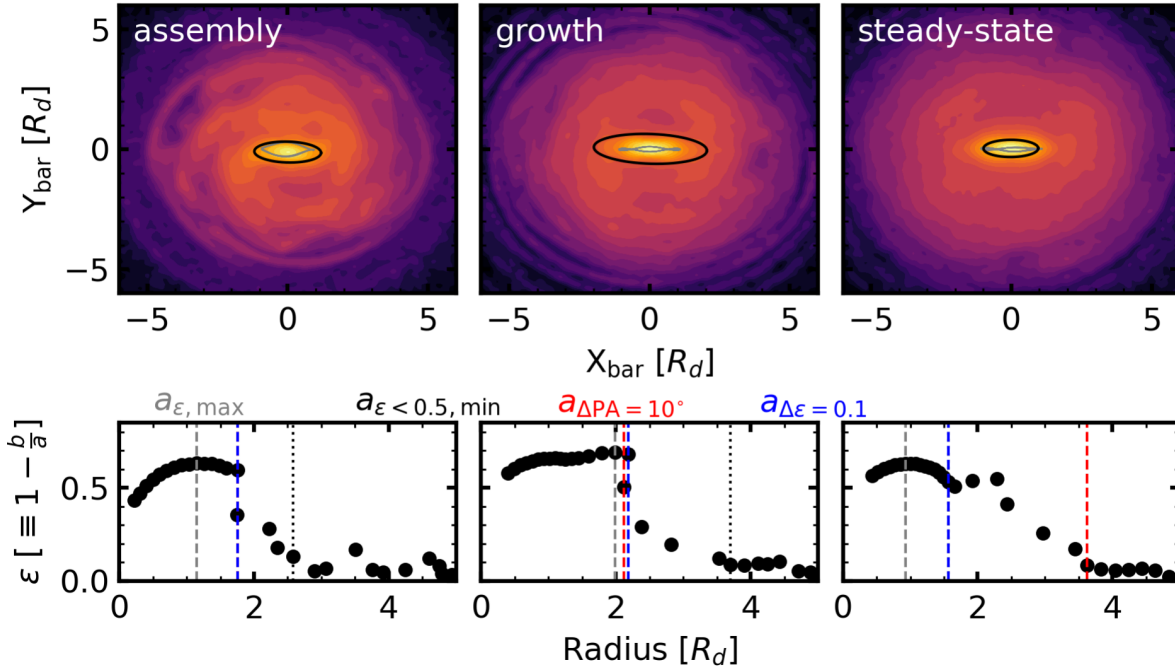


**Figure B1.** Upper row: three face-on surface density snapshots extracted from the simulation, at different phases of bar evolution. Lower row: eccentricity vs major axis for ellipses drawn to match isophotes in the surface density snapshots. We also demonstrate different ellipse-fitting methods and the results for bar length (grey, black, red, and blue vertical lines, using the methods indicated above the panels).

orbit identified by the  $k$ -means classifier, relative to the maximum-ellipticity ellipse. In some cases, the maximum-ellipticity ellipse is a good match, but this appears to be purely coincidental, as demonstrated by the poor match during the growth phase.

### APPENDIX C: A SAMPLE OF ISOLATED GALAXY SIMULATIONS

To probe a wider range of bar models, and test the robustness of our technique to measure the dynamical length, we generate a new sample of barred galaxies by varying the concentration in a NFW (Navarro et al. 1997) dark matter halo. The dark matter density affects the formation, structure, and evolution of bars in galaxies (see, e.g. Debattista & Sellwood 2000). We effectively increase and decrease the dark matter density in the disc region by changing the concentration of the dark matter halo compared to the original model of Petersen et al. (2021), which had  $c = 15$ , using  $c = [5, 10, 15, 20, 25]$  to span a very large range of NFW halo models. The models are denoted by their concentration, e.g.  $c5$  for the  $c = 5$  model.

The models follow the initial condition generation procedure described in Paper I, with the only change being the scale height: in the newly-generated sample we choose a ratio of  $z_d/R_d = 0.15$ , in contrast to the primary model presented in this paper, which has  $z_d/R_d = 0.1$ . The increase in scale height of the model makes the disc more in line with estimates for the structure of the Milky Way thin disc ( $h_{\text{scale}} = 0.0015$  in virial units, or 450 pc when scaled to the Milky Way, cf. Petersen et al. 2021). All new models are run for  $T_{\text{vir}} = 5$ , using the same settings as in Paper I for the cusp model. Each model forms a bar that then evolves. The bars span a relatively broad set of morphologies: from shorter more compact

bars to highly elongated bars. We track the length of the  $x_1$  orbit family in the live simulation in the same manner as described in the main text.

Figure C1 shows each galaxy model ( $c5$ ,  $c10$ ,  $c15$ ,  $c20$ ,  $c25$ , in columns) in snapshots at four times ( $T = 1.2$ ,  $T = 2.0$ ,  $T = 2.8$ ,  $T = 3.6$ , in rows). The snapshots demonstrate the breadth of the bar morphologies that we test. For each of these twenty snapshots, we perform an ellipse fit to the face-on image. A selection of resultant ellipses are shown overlaid on each image. From a full set of ellipse fits, we determine the semi-major axis of the maximum ellipticity ellipse, and compute the ratio of this semi-major axis to the maximal  $x_1$  length as the ‘ellipse-derived ratio’. We plot these values as the  $x$ -axis of Figure C2, and show they consistently overestimate the bar length (excepting one failed ellipse-determination), with a mean overestimate of 2x. As an estimate of the uncertainty, we take the semimajor axis of the ellipse fit to a log10 isophotal value that is 10 per cent larger. This results in an approximately 20 per cent uncertainty estimate on the ellipse-derived length. The uncertainty in the maximal  $x_1$  length is much smaller than the ellipse semi-major axis uncertainty and, therefore, we only indicate the ellipse uncertainty in Figure C2.

We also perform the Fourier-velocity bar length measurement for each sample snapshot, and compute the ratio of the derived length to the  $x_1$  length. This is the  $y$ -axis in Figure C2. Here, we see that the measurements are clustered around unity, indicating that the velocity method recovers the  $x_1$  length in this sample of snapshots. As an estimate of the uncertainty, we follow the same procedure as in the main text and compute the minimum for a variety of bin sizes and numbers. We then take the points and fit a negative Gaussian, using the standard deviation of the fit as the uncertainty on the velocity-derived length. This typically yields 10 per cent uncertainties.



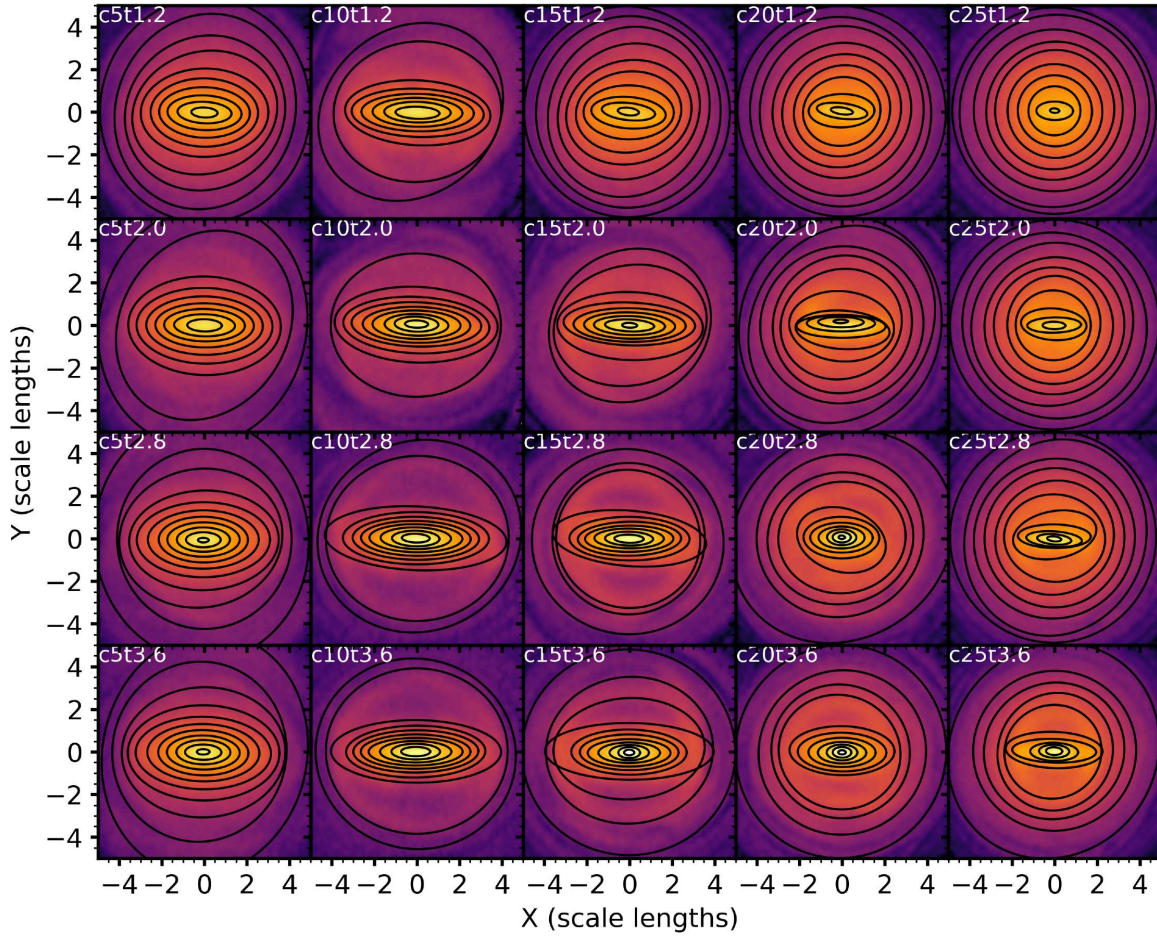


**Figure C1.** Face-on snapshots of five different galaxy models (columns) at four different times (rows). The models are described in the text and are designed to show a range of bar and disc morphologies in isolated galaxies. On each panel, we overlay a handful of indicative ellipse fits to the isophotes, as black curves.

Overall, we find that the velocity-derived metric consistently returns a bar length that is comparable to the dynamical length. We acknowledge that the bar morphology in these models is not necessarily a representative sample of the observed morphologies found in the real Universe. Future work could additionally test our technique on cosmological simulations, where bars may be directly caused by interactions, resulting in a broader set of morphologies. However, our snapshots do demonstrate that the velocity method works for a wide range of isolated barred galaxy models, with essentially zero failures, even in the case of very weak bars (e.g. *c25t1.2*).



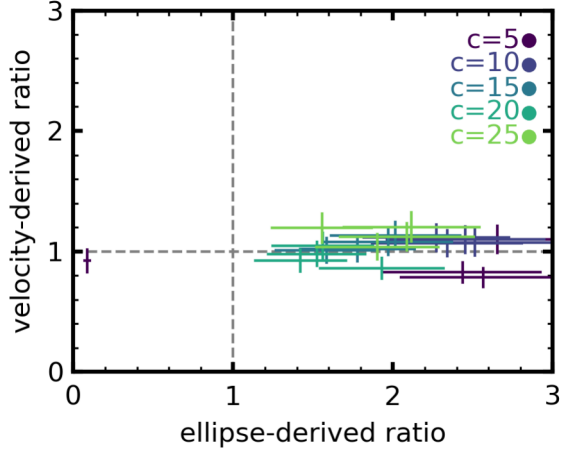


**Figure C2.** The ratio of the maximum-ellipticity semimajor axis to the determined maximal  $x_1$  length ('ellipse-derived ratio') versus the ratio of the  $x_1$  velocity derived length to the maximal  $x_1$  length ('velocity-derived ratio'). The velocity-derived ratio consistently returns a value near the maximal  $x_1$  length. Different colour points correspond to different models (darkest are  $c=5$ , lightest are  $c=25$ , marked in the legend). Each point carries an uncertainty estimate derived from repeated observations while changing parameters; the uncertainty in the ellipse-derived ratio is approximately 20 per cent and the uncertainty in the velocity-derived ratio is approximately 10 per cent.